33RD CONGRESS
OF THE INTERNATIONAL COUNCIL
OF THE AERONAUTICAL SCIENCES
STOCKHOLM, SWEDEN, 4-9 SEPTEMBER, 2022

ICAS
2022
SWEDEN

INFLUENCE OF KEYHOLE TIG WELDING PARAMETERS ON WELD GEOMETRY OF NEWLY-DEVELOPED SUPERALLOY VDM ALLOY 780

Achmad Ariaseta[1,2]*, Nima Sadeghinia[1], & Joel Andersson[1]

[1]Department of Engineering Science, University West, SE-46186 Trollhätan, Sweden
[2]Department of Metallurgical Engineering, Faculty of Mining and Petroleum Engineering, Institut Teknologi Bandung, Jl. Ganesha 10, Bandung 40132, Indonesia

Abstract

The welding process and the associated control, to a certain degree, have enhanced remarkably in the last decades. One of the recent processes is keyhole TIG (K-TIG) welding, which allows better control and the capability to use lower heat input and higher power density during the welding compared to the conventional one, being essential when joining sophisticated materials utilized in the hot sections of aircraft engines such as nickel-based superalloys. The recent trend in the fabrication of hot sections of aero-engines has been preferably carried out by joining small pieces of superalloys by the welding process instead of casting a single large component due to several benefits, such as lowering the total weight of the components and improving the design flexibility. VDM Alloy 780, a new polycrystalline nickel-based superalloy with service temperature capabilities up to 750 °C, is a promising material to be employed in the fabrication of hot structural parts of an aero-engine. For aerospace manufacturers, producing a superalloy weld bead geometry that meets stringent quality requirements for aerospace applications is crucial. To do so, understanding the influence of welding parameters on weld geometry becomes indispensable, especially when welding a new superalloy using a relatively new welding technique. Hence, in this article, the influence of K-TIG welding parameters on the weld geometry of VDM Alloy 780 has been investigated.

Keywords: K-TIG welding; welding parameters, weld geometry; VDM Alloy 780

1. Introduction

Superalloys are materials that possess outstanding properties at high temperatures – i.e., high-temperature strength, corrosion, and creep resistance. They are commonly nickel (Ni), nickel-iron (Ni-Fe), cobalt (Co), or even nickel-cobalt (Ni-Co)-based types [1-4]. Nickel-based superalloys are classified into three groups based on their strengthening mechanism: solid-solution, precipitation, and oxide dispersion strengthening (ODS) superalloys. Precipitation strengthening types are the ones that are widely used in the hot structural parts of aircraft engines. Precipitation-strengthening nickel-based superalloys consist of γ FCC matrix and secondary phases such as carbides, nitrides, borides, and strengthening precipitates in their microstructure. Strengthening precipitates that are commonly observed in precipitation-hardening superalloys are gamma-prime γ' (Ni_3(Al, Ti) and gamma-double prime γ''(Ni_3Nb). The examples of superalloys strengthened by γ' are Haynes 282, Waspaloy, and ATI 718Plus. Alloy 718 is an example of γ''-strengthening superalloy.

VDM Alloy 780 is a γ'-hardening nickel-based superalloy recently developed by VDM Metals International to enhance the maximum service temperature while maintaining the fabricability of Alloy 718 [4, 5]. The development of VDM Alloy 780 is accomplished by having significant differences to Alloy 718 in chemical composition, which are the addition of 25% Co substituting Ni and Fe, increased amount of Al (2% instead of ~0.6%), decreased amount of Ti (0.2% instead ~0.94%) [6]. The amount of Nb, Cr, and Mo is maintained as those of Alloy 718. The alloy development strategy results in the γ' phase being the principal hardening phase, which enhances its thermal stability in comparison to Alloy 718, which is strengthened by γ''. The significant Co content in the alloy, which exceeds Co content in ATI 718Plus (9%) and Waspaloy (13%), together with low Ti/Al lead to the notable γ' strengthening in VDM Alloy 780 [6]. The overall results are a higher volume fraction of γ', more sluggish γ' precipitation kinetics, lower γ' solvus temperature in the range of 995 to 1000 °C [7], and higher strength than that of Waspaloy as a classical γ' precipitation hardening superalloy [6].

VDM Alloy 780 is a promising superalloy to be used in the fabrication of aero-engine hot sections. The hot sections of aero engines have been preferably fabricated by welding small pieces of superalloys instead of casting a single large components. The fabrication strategy has several benefits, such as increasing the design flexibilities, e.g., it becomes possible to join cast (complex geometry) alloys with wrought (high strength) alloys and also join different superalloys [8]. Another benefit is reducing the component's total weight, enhancing the engine's fuel efficiency, and eventually less CO_2 emission to the environment.

One of the most standard techniques employed in the fabrication of hot sections of the aero-engine in the aerospace industry is tungsten inert gas (TIG) welding [9]. However, TIG welding processes have undergone notable improvements that paved the way for the fabrication of structural components of the jet engines, and now possible to use lower heat input. Recently, a new high-performance TIG welding process called keyhole TIG (K-TIG) was developed. K-TIG welding has the capability to achieve a keyhole or full penetration in a single-pass with lower heat input and faster travel speed compared to the traditional TIG due to a highly concentrated arc with high power density.

From an industrial point of view, producing a superalloy weld that meets the tight industrial quality requirement in the aerospace industry in terms of weld geometry is critical. Since VDM Alloy 780 is a new alloy, and K-TIG welding itself is a relatively new welding technique, no reports from the literature regarding the effect of process parameters on the weld geometry. Hence, the article aims to study the influence of K-TIG welding process parameters on the weld geometry of VDM Alloy 780.

2. Experimental Procedure

2.1 Material and Welding

VDM Alloy 780 plates in solution-annealed condition with a thickness of 5.7 mm were used for the bead on plate weld runs using the robotic K-TIG welding machine. The 99.99% purity argon gas was employed as the shielding gas with a flow rate of 10 ml/min through the copper pipe. The schematic of the bead on plate weld run on the VDM Alloy 780 plates is shown in Figure 1. The chemical composition of the VDM Alloy 780 plate used in this study is displayed in Table 1. The methods used were combustion analysis (C, S, N, and O), X-ray fluorescence spectroscopy (Cr, Mn, Mo, Si, Nb, Ti, Cu, Fe, Al, V, W, Co, and Zr), optical emission analysis (P, Mg, and B), graphite furnace AAS (Pb, Sn, As, Se, Te, Bi, and Ag), flame AAS (Ca), and inductive coupled plasma (Ta).

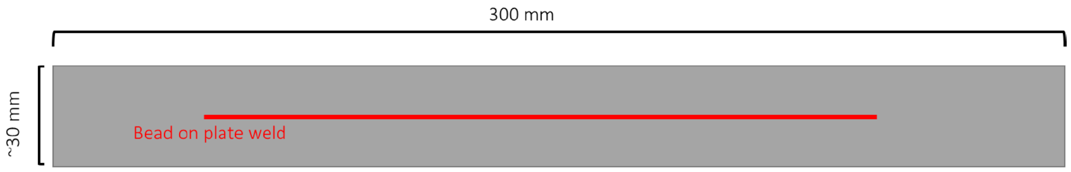

Fig. 1 The schematic of bead on plate weld run on the VDM Alloy 780 plates.

Table 1 – Chemical compositions, in wt%, of VDM Alloy 780 used in the present study.

Element	Ni	Al	Ti	Nb	S	Cr	Sn	V	Zr	Mo	Co	Cu
wt%	Bal.	2.19	0.30	5.39	0.0005	17.95	<0.001	0.01	<0.01	2.91	25.08	0.01

Element (cont.)	Si	Mn	C	P	Ta	Se	Mg	B	N	O	Fe
wt% (cont.)	0.03	0.01	0.021	0.01	0.01	<0.0003	0.0006	0.003	0.008	0.001	0.47

Element (cont.)	W	Ca	Se	As	Sb	Ag	Te	Bi
wt% (cont.)	0.02	0.002	<0.0003	<0.001	<0.0005	<0.0001	<0.00005	<0.00003

2.2 Statistical Design of Experiment (DOE)

The DOE employed to investigate the influence of K-TIG welding process parameters on weld geometry in this work was based on a two-level full factorial experiment with the two factors, i.e., welding current and travel speed. Hence, the DOE will create four different combinations of the welding parameters. Three middle points, i.e., Samples 5, 6, and 7, were added, which resulted in seven experiments. The levels specified for welding parameters with their units and levels are given in Table 2. The current and travel speed ranges were selected to acquire full penetration without burning through the VDM Alloy 780 plate. The gap between the tip of the electrode and the plate was constant at 1.5 mm. After welding, the typical weld geometry features specified in AWS D17.1M:2010 [10] as the responses were measured, i.e., face excess weld metal, root excess weld metal, and underfill. Then, the results were input into Modde software (MODDE 12, Umetrics, Umeå, Sweden) and shown in the last three columns of Table 3. Linear regression was utilized to model each response according to equation (1) as follows.

$$y = \beta_0 + \beta_1 x_1 + \beta_2 x_2 + \beta_{12} x_1 x_2 + \varepsilon \qquad (1)$$

where y is the response, which is the dependent variable; the β terms are constants, of which all excluding β_0 are called regression coefficients; the x terms are the independent variables expressing the levels of a factor; here, for example, x_1 and x_2 represent the levels of welding current and travel speed, respectively. Furthermore, the combination of x_1x_2 describes the interaction of welding current and travel speed. The parameter levels defined by x were expressed on a coded scale. Here, 480, 485, and 490 A for the welding current levels are coded −1, 0, and 1, respectively. While for the travel speed levels, 8, 8.5, and 9 mm/s are coded −1, 0, and 1, respectively. ε is the standard error. The coefficients were computed by the multiple linear regression (MLR) method together with their 95% confidence intervals. A square test was also carried out in the Modde software to detect any square terms or non-linearity. No non-linearity was detected in the square test in all response regression models in this work.

Other diagnostic parameters that were also calculated in the Modde software were R^2, P-value, and reproducibility. R^2 is a diagnostic parameter that determines how much the output variation is explained by a regression model's input(s) variation, and the range is from 0 to 1. In the case of a high R^2 value, the predicted vs. measured plot points are closer to the straight line. The P-value was calculated by generating an analysis of variance (ANOVA) table. If $P\text{-value} < 0.05$, there is a significant relationship between factors and response, rejecting the null hypothesis. The null hypothesis is defined in Equation 2. The other diagnostic parameter, i.e., reproducibility, was measured by comparing the variation of the middle points (replicates) with the variation of the main runs. It implies the reproducibility of the test, and the range is from 0 to 1, in which values larger than 0.5 indicates good reproducibility [11].

$$\mathrm{H_0}: \beta_1 = \beta_2 = \beta_{12} = 0 \qquad (2)$$

Table 2 – K-TIG welding parameters and their levels.

No.	K-TIG welding parameters	Units	Welding parameter levels		
			-1	0	1
1	Welding current	A	480	485	490
2	Travel speed	mm/s	8	8.5	9

Table 3 – Full factorial experiment of K-TIG welding and the measured weld geometry responses.

Experiment no.	Current (A)	Travel speed (mm/s)	Face underfill (mm)	Face excess weld metal (mm)	Root excess weld metal (mm)
1	480	9	0	0.404	0.71
2	490	8	0.084	0.328	0.874
3	480	8	0.094	0.104	1.146
4	490	9	0.01	0.43	0.888
5	485	8.5	0.018	0.366	0.838
6	485	8.5	0.026	0.286	0.974
7	485	8.5	0.008	0.312	0.884

2.3 Weld Geometry Measurement

Five transverse cross-sections were sliced from all the DOE K-TIG weld runs in the middle of the plates. The mounted cross-sections were prepared by standard metallographic preparation involving multi-step grinding and polishing. Electrolytic etching using 10% oxalic acid at 2.5 V for about two seconds was conducted to disclose the bead geometry. Macro images of the weld cross-sections were then captured on etched samples using an optical microscope to acquire accurate measurements of face underfill and excess weld metal on the face and the root. The values were averaged from five cross-sections. An example of a macro image of bead geometry and the corresponding measurements are displayed in Figure 2. The face underfill, face, and root excess weld metal measured in the DOE runs in this work were compared with the maximum allowable limit specified in AWS D17.1M:2010 [10].

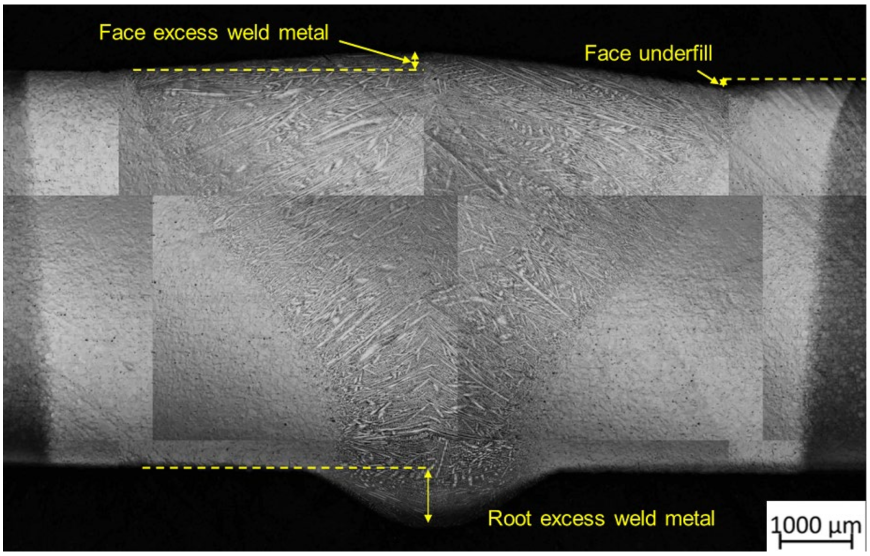

Fig. 2 – Macro image displaying the example of bead geometry and the measurements.

3. Results and Discussion

3.1 Face underfill

The extent of face underfills of Samples 1–7 are shown in Figure. 3. These data were taken directly from Table 2. The middle points, i.e., Samples 5–7, displayed reasonably similar values. This was reflected in the calculated reproducibility value of 0.95. Furthermore, all the DOE runs produced welds with the face underfill lower than the maximum acceptable limit specified in AWS D17.1M:2010 [10] for aerospace applications shown in red dotted line in Figure 3.

The interaction plot of welding current and travel speed on the face underfill was analyzed in Modde and is depicted in Figure 4. The initial observation was that there was no apparent interaction between the current and travel speed, as the green and blue speed plots were parallel. Figure 4, however, displays that the extent of face underfill increased with decreasing speed. It is essential to know which of the K-TIG welding parameters had the most substantial influence on the face underfill and whether there were any significant interactions among these welding parameters. Hence, regression coefficients calculated in Modde are presented in Table 4. The significant parameters with P-value < 0.05 are labeled in green, while those with no significant P-value ≥ 0.05 that included zero in their 95% confidence intervals are labeled in red. All the coefficients are plotted in Figure 5 and depicted with their 95% confidence intervals. It is shown that travel speed significantly influenced face underfill. It can be interpreted that the travel speed significantly influenced the face underfill. The interaction current*travel speed was not statistically significant

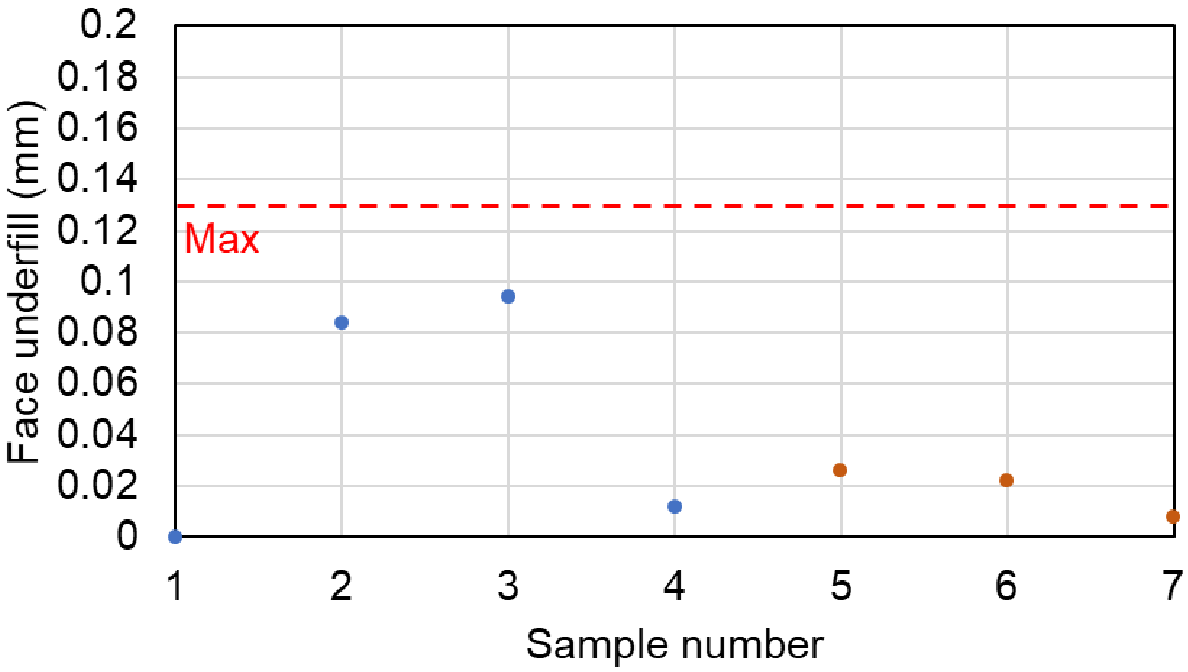

Fig. 3 – Measured face underfill of welded samples (samples with varied parameters are in blue, while replicates are in orange); The face underfill was compared with the maximum allowable limit specified in AWS D17.1M:2010 (shown in red dotted line)

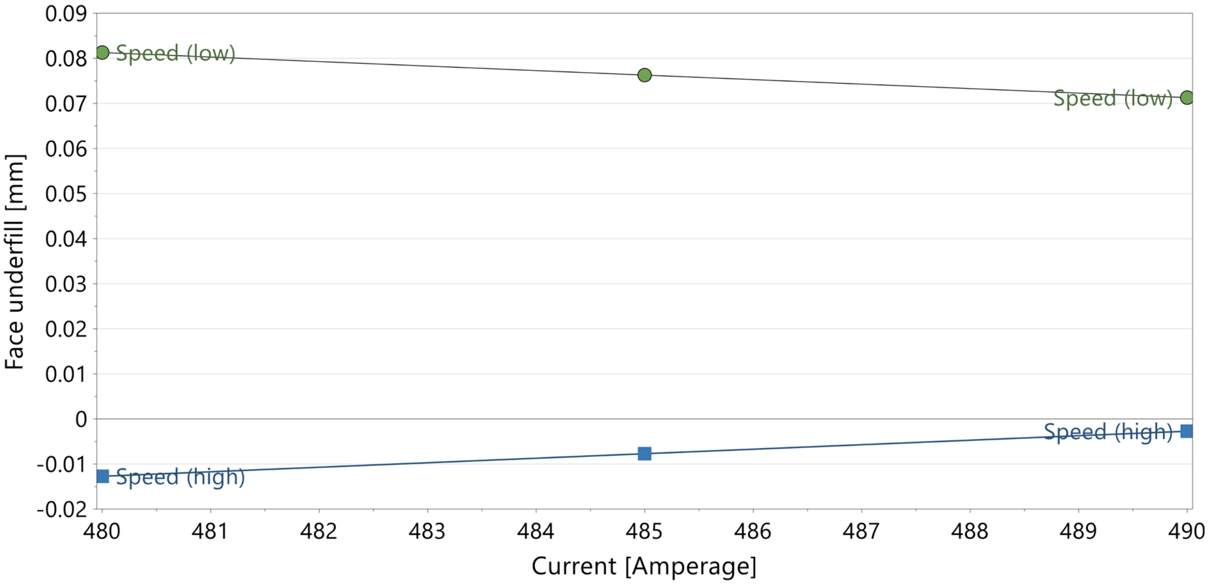

Fig. 4 – Welding current and travel speed interaction plot on the face underfill

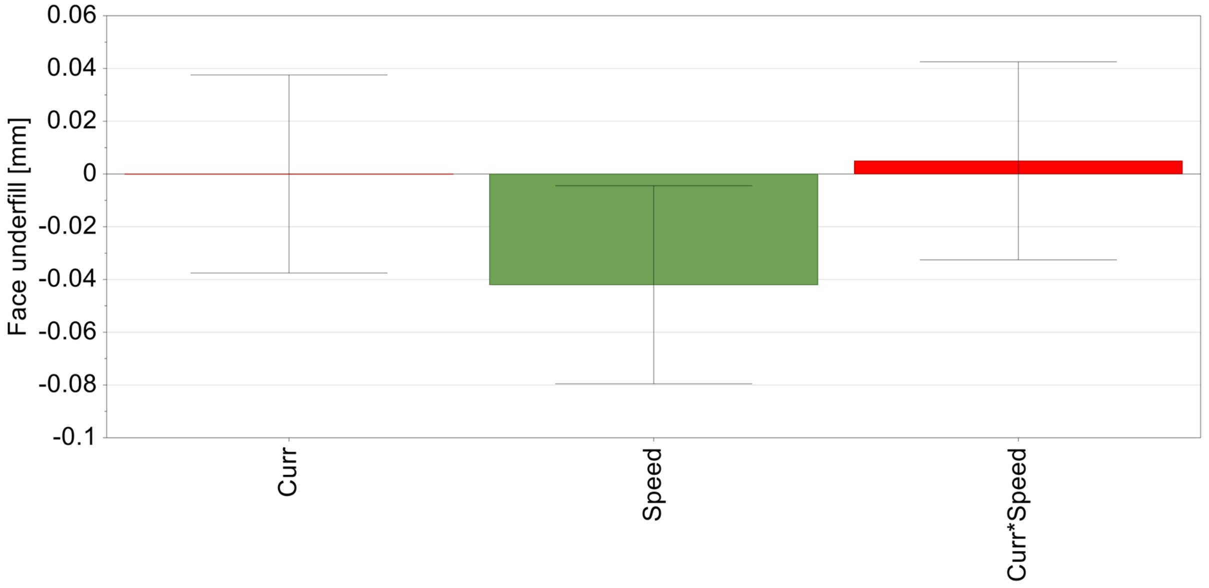

Fig. 5 – Regression coefficients for different factors and interaction of factors influencing underfill (green bars display significant factors, while red bars display non-significant factors).

Table 4 – P values calculated using Modde software for the regression constants that had significant (significant values are marked in bold) and non-significant influence on the face underfill.

Factors	Constant	Coefficient	P-value
	β_0	0.0342857	0.031085
Current	β_1	2.50964e-09	1
Travel speed	β_2	-0.042	**0.0378542**
Current*travel speed	β_{12}	0.005	0.700355

The next stage is to know how experimentally measured face underfill in the K-TIG welded sample compared with the calculated values of the regression model. The regression model of face underfill is shown in Equation 3. It is worth reminding that the x variables were represented in a coded scale as described in the experimental procedure. A plot comparing the measured face underfill and calculated face underfill is shown in Figure 6. The line intersects the points where the measured values are equal to the calculated values. The R^2 value of face underfill was 0.81. Although the R^2 of the regression model was reasonably high at 0.81, it can be seen from Figure 9 that the measured values did not accurately match the calculated values. The model showed a significant lack of fit, which was indicated in the ANOVA table generated in Modde. In Figure 6, it is apparent that negative values were predicted. This does not mean that a negative value of face underfill was present. In actuality, the measured values were near zero, which, along with a lack of fit, made it possible to generate or predict negative values numerically. In addition, from the ANOVA table, the P-value of the regression model was 0.132, suggesting that the model was statistically poor or not significant.

$$y = 0.05842857 + 2.50964e - 09x_1 - 0.042x_2 + 0.005\,x_1x_2 \tag{3}$$

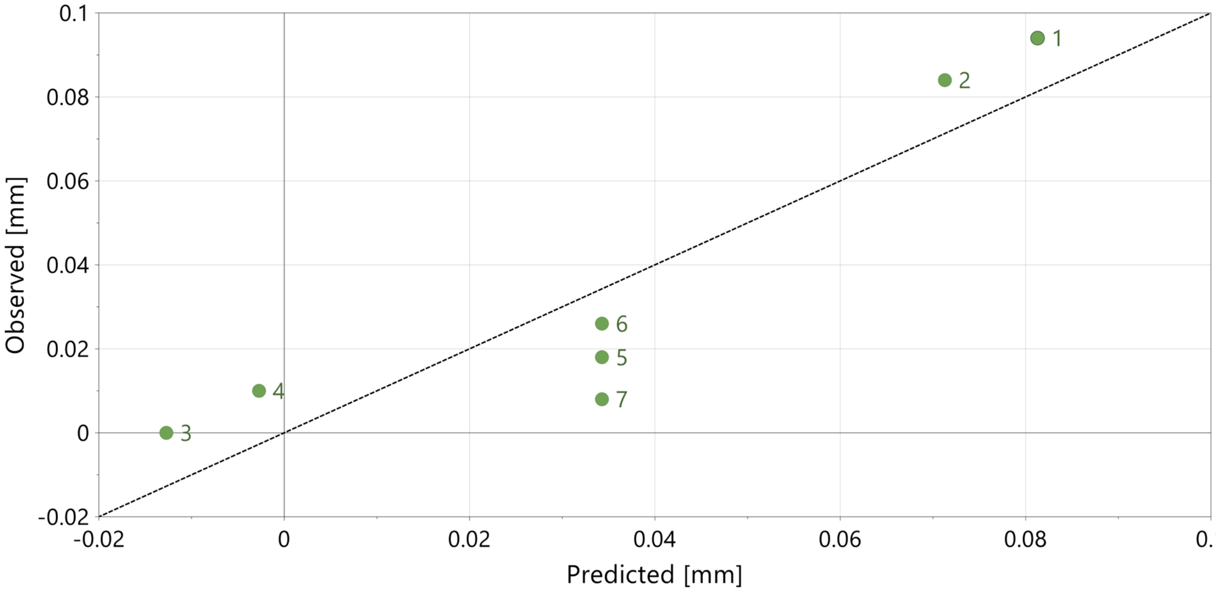

Fig. 6 – Comparison of all experimentally measured face underfill with the predicted results from the regression model.

3.2 Face excess weld metal

As seen in Table 2 and shown in Figure 7, the face excess weld metal was lower than the maximum acceptable limit stipulated in AWS D17.1M:2010 [10] for aerospace applications. Samples 5, 6, and 7 displayed face excess weld metals which were reasonably close to each other, which was again reflected with the reproducibility value of 0.86.

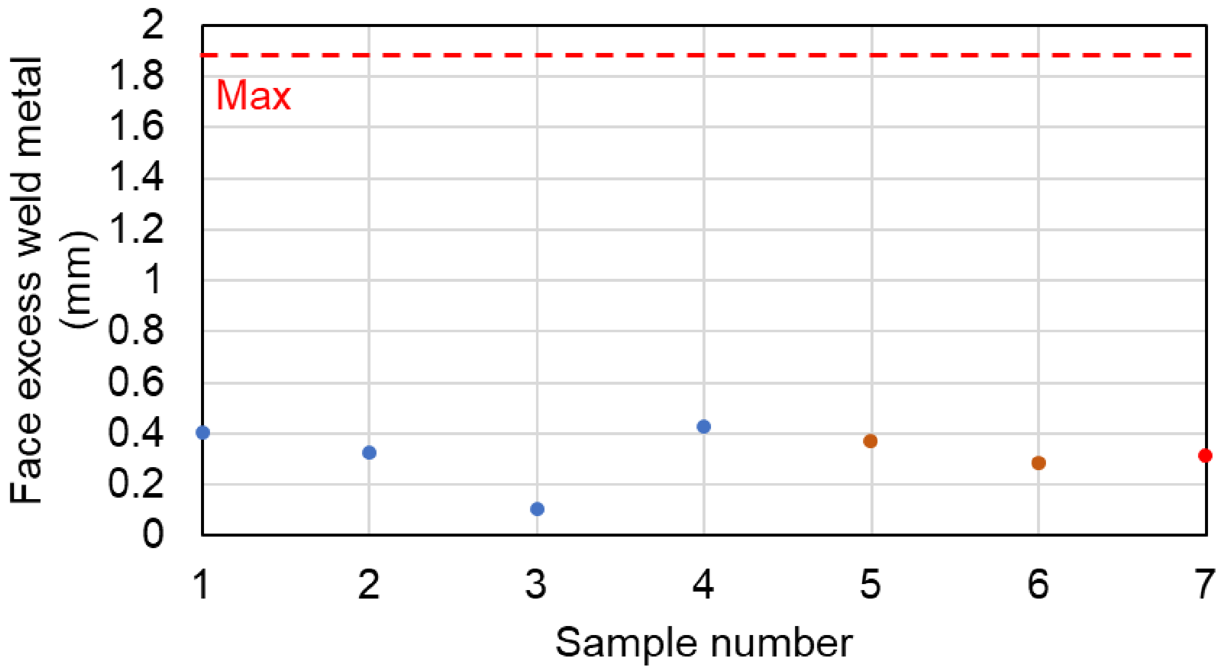

Fig. 7 – Measured face excess weld metal of welded samples (samples with varied parameters are in blue, while replicates are in orange); The face excess weld metals were compared with the maximum allowable limit specified in AWS D17.1M:2010 (shown in red dotted line)

Figure 8 displays the interaction plot of welding current and travel speed on the face weld metal. Here, it is evident that lower speed led to lower face excess weld metal. At first, there seemed no notable change of face excess weld metal when the current was increased at high travel speed. However, at low travel speed, higher welding current led to higher face excess weld metal. Based on this trend, one might interpret that there was a significant interaction of welding current*travel speed. Nevertheless, it was evident in the coefficient plot (Figure 9) and P-value (table 5) that there was no significant welding current and travel speed interaction, as shown regression coefficient plot that confidence intervals had zero included and P-values higher than 0.05. This was due to the P-value of the interaction of welding current*travel speed that was slightly higher than 0.05, which might lead one to interpret significant interaction effect was likely to exist. Instead, Figure 9 and Table 5 revealed that welding current was observed to be statistically significant. It was confirmed from Figure 9 and Table 5 that travel speed was statistically significant, and it showed the strongest influence on the face excess weld metal.

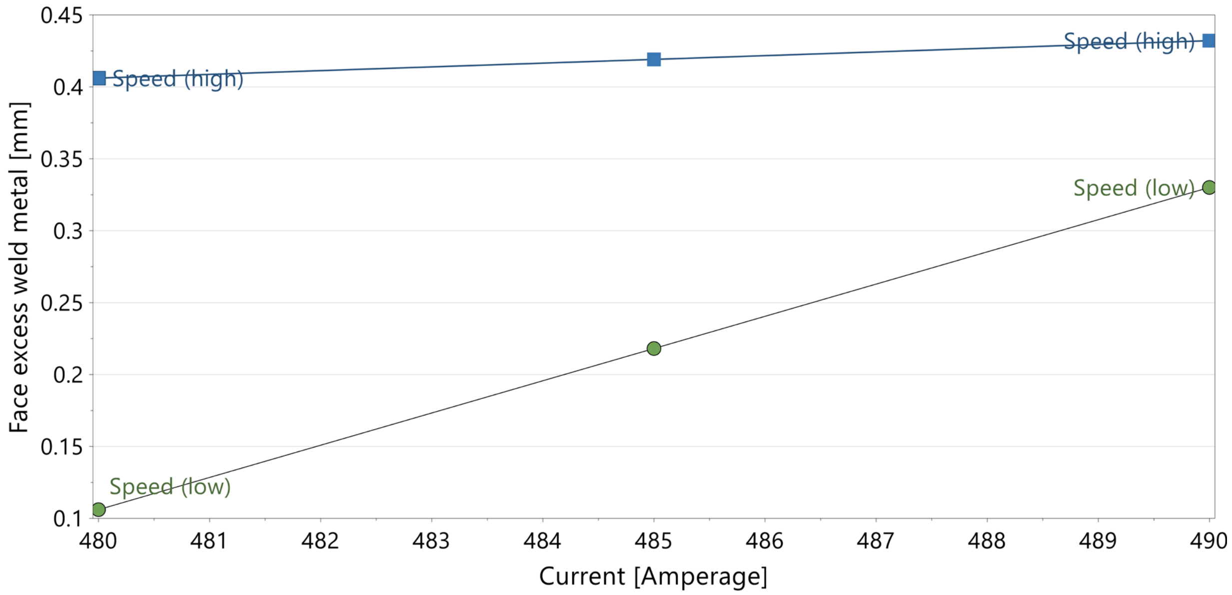

Fig. 8 – Welding current and travel speed interaction plot on the face excess weld metal

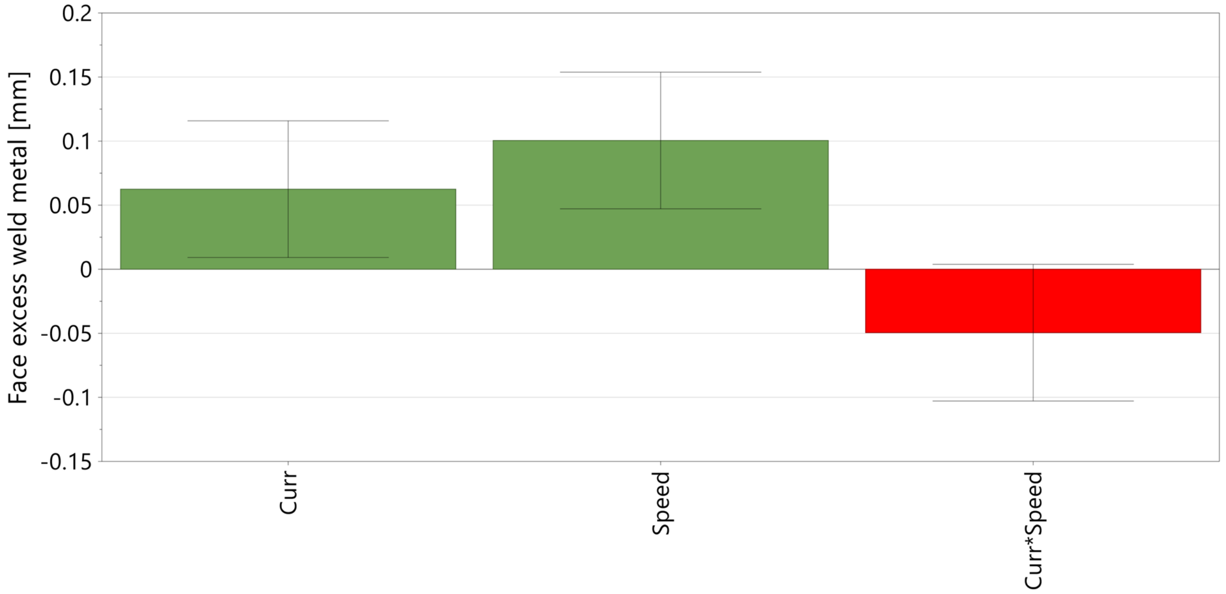

t

Table 5 – P values calculated using Modde software for the regression constants that had significant (significant values are marked in bold) and non-significant influence on face excess weld metal

Factors	Constant	Coefficient	P-value
	β_0	0.318571	0.000137923
Current	β_1	0.0625	**0.0335945**
Travel speed	β_2	0.1005	**0.00928808**
Current*travel speed	β_{12}	-0.0495	0.0598566

A comparison of the measured face excess weld metal to the calculated values is depicted in Figure 10. The regression model was fitted as shown in Equation 4. Here, the R^2 value was 0.95. This is evident from Figure 10 that the points are very close to the 1:1 line, indicating a good fit. The calculated P-value of the regression model from the ANOVA table was 0.018. This suggests that the model was statistically significant.

$$y = 0.352091 + 0.0625x_1 + 0.1005x_2 - 0.0495\, x_1x_2 \tag{4}$$

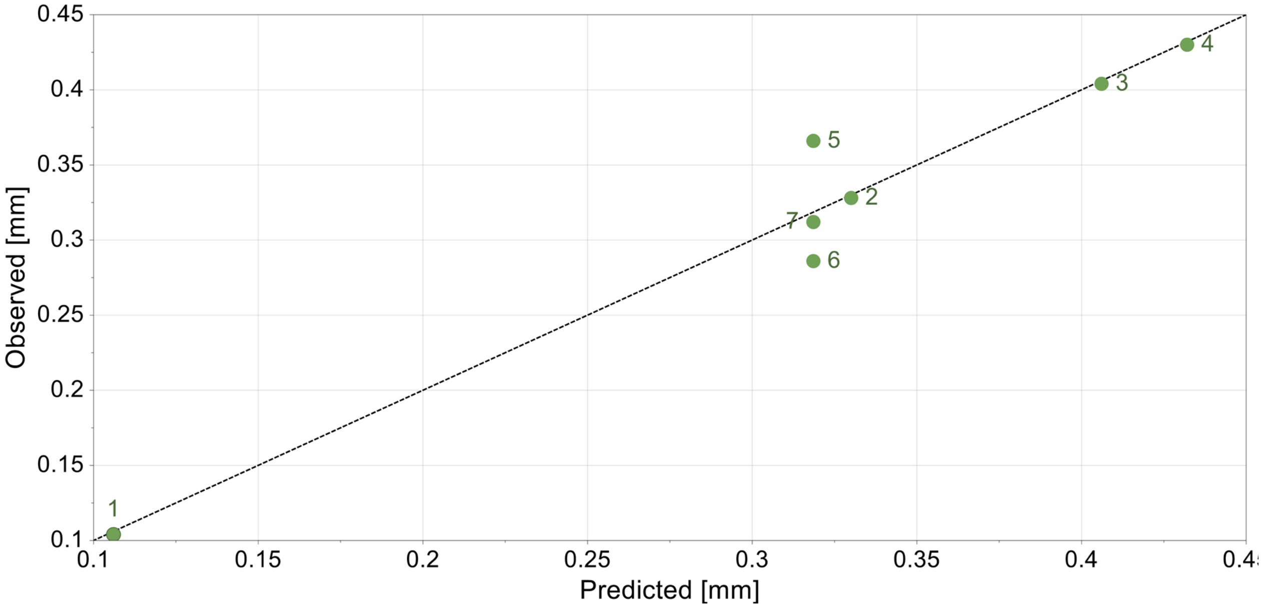

Fig. 10 – Comparison of all experimentally measured face excess weld metal with the predicted results from the regression model.

3.3 Root excess weld metal

The measured root excess weld metal of Samples 1–7 are displayed in Figure 11. The middle points, i.e., Samples 5–7, also showed reasonably similar values. The calculated reproducibility value was 0.73, which was lower than the reproducibility values of face underfill and face excess weld metal. However, the value was still higher than 0.5, suggesting a relatively good reproducibility. All the DOE runs also produced welds with the root excess weld metal lower than the maximum acceptable limit specified in AWS D17.1M:2010 for aerospace applications

The interaction analysis in Modde for welding current and travel speed is depicted in Figure 12. What is immediately apparent is the significance of current*travel speed interaction, which is why the plots cross each other at some points. It reveals that the trend of root excess weld metal (the slope of each plot) of the current depends on the level of the travel speed. The face underfill plots of the current and travel speed displayed earlier in Figure 4 did not cross each other because their interactions were not substantial. The significant interaction of current*travel speed was confirmed in the coefficient plot (Figure 13), and its value was higher than 0.05 (Table 6). Here, the interaction of current*travel speed was the strongest process parameter influencing the root excess weld metal. Figure 13 and Table 6 also depict that travel speed significantly influenced the root excess weld. On the other hand, the welding current did not significantly influence the root excess weld metal.

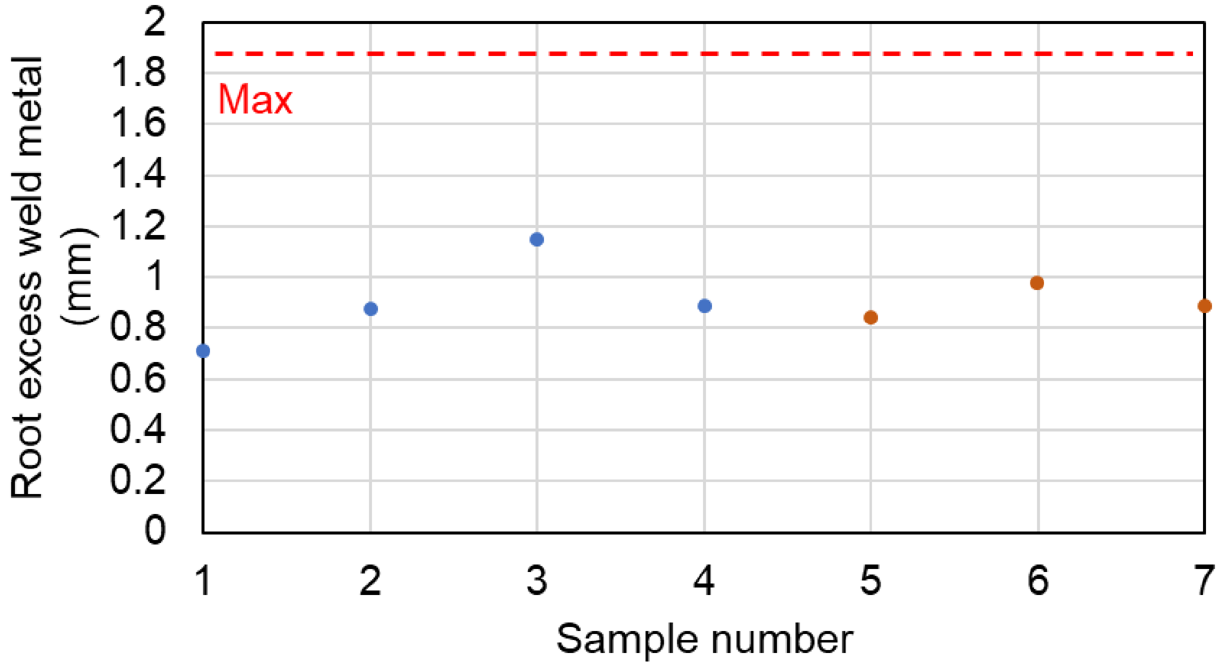

Fig. 11 – Measured root excess weld metal of welded samples (samples with varied parameters are in blue, while replicates are in orange); The face excess weld metals were compared with the maximum allowable limit specified in AWS D17.1M:2010 (shown in red dotted line)

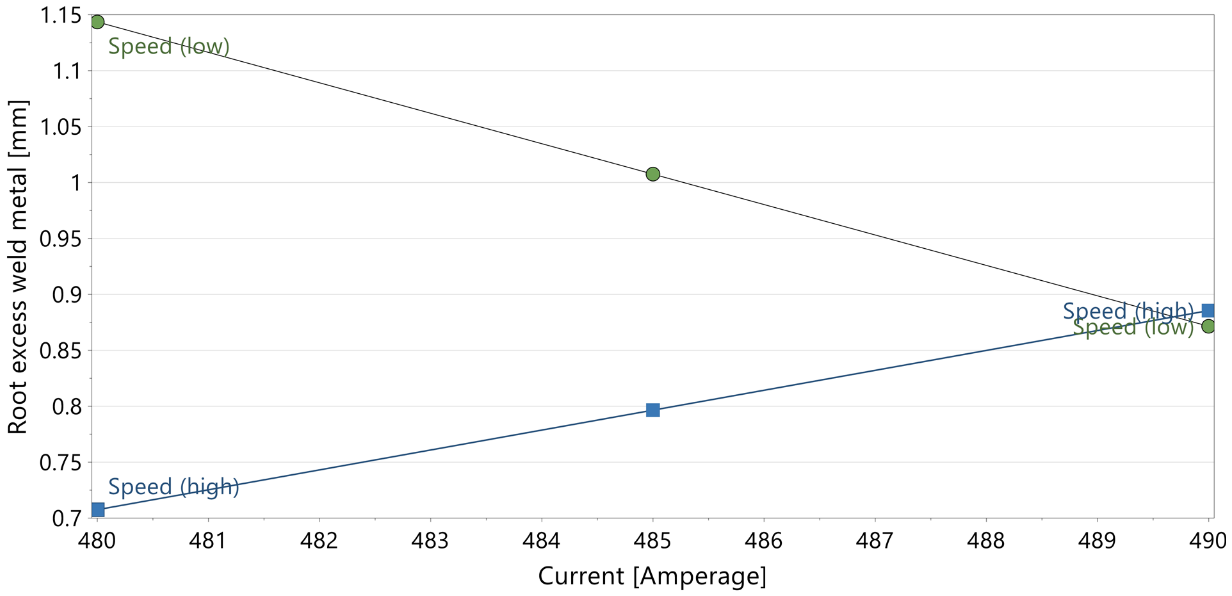

Fig. 12 – Welding current and travel speed interaction plot on the root excess weld metal

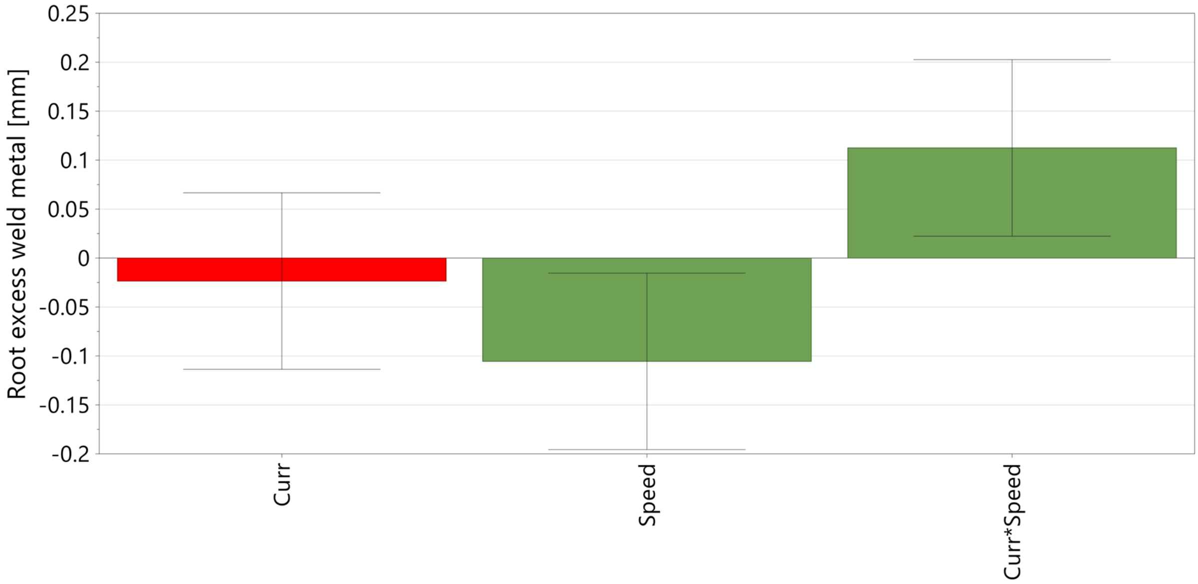

Fig. 13 – Regression coefficients for different factors and interaction of factors influencing root excess weld metal (green bars display significant factors, while red bars display non-significant factors).

Table 6 – P values calculated using Modde software for the regression constants that had significant (significant values are marked in bold) and non-significant influence on the root excess weld metal.

Factors	Constant	Coefficient	P-value
	β_0	0.902	2.94451e-05
Current	β_1	-0.0235	0.467612
Travel speed	β_2	-0.1055	**0.0337055**
Current*travel speed	β_{12}	0.1125	**0.0285374**

The plot of the experimentally measured values of root excess weld metal compared to the calculated values is shown in Figure 14. The regression model was fitted as shown in Equation 5. Here, the calculated R^2 was 0.91, indicating that the experimental results were close to the calculated values. From Figure 13, the points were crossed by the 1:1 line, suggesting a good fit. The P-value of the regression model was 0.045, indicating the model was statistically significant

$$y = 0.95865 - 0.0235x_1 - 0.1055x_2 + 0.1125\, x_1x_2 \tag{5}$$

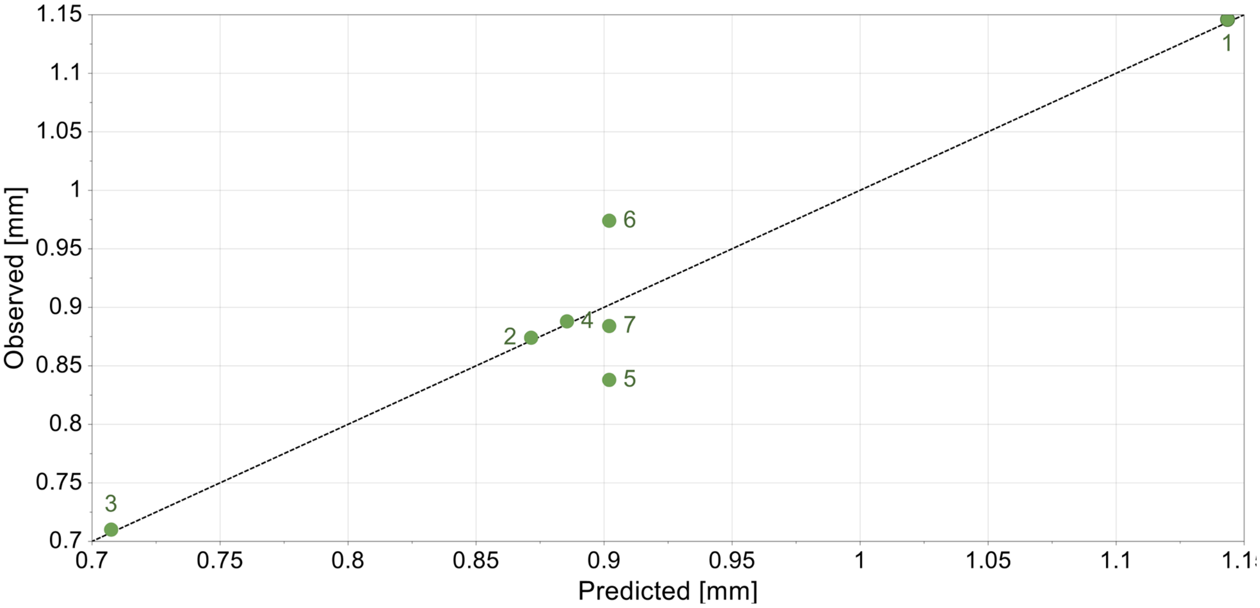

Fig. 14 – Comparison of all experimentally measured root excess weld metal with the predicted results from the regression model.

4. Conclusions

1. All the welds produced in the K-TIG DOE runs in this study had face underfill, face excess weld metal, and root excess weld metal lower than the maximum acceptable limit specified in AWS D17.1M:2010 for aerospace applications.
2. Face underfill was only significantly influenced by travel speed, and no significant influence of welding current and interaction of welding current and travel speed was observed. Lower face underfill may be obtained by increasing the travel speed
3. Face excess weld metal was significantly influenced by welding current and travel speed. Lower face excess weld metal may be obtained by decreasing the travel speed and/or welding current
4. Root excess weld metal was significantly influenced by travel speed and interaction of current*travel speed. The interaction of current*travel speed was the strongest process parameter influencing the root excess weld metal. Lower root excess weld metal may be obtained by increasing the travel speed and decreasing the current.
5. The regression model of face underfill was statistically poor or not significant despite a reasonably high R^2 value of 0.81.
6. The regression models of the face and excess weld metal were statistically significant, with both exhibiting high R^2 values of 0.95 and 0.91, respectively.

.

5. Acknowledgment

This work is based on the research within the FEAST (Weld Feasibility Heat Treatment Studies of New Superalloys, registration number: 2019-02787) project funded by the Swedish funding agency VINNOVA. We highly appreciate the support and input from Dr. Ceena Joseph, Mr. Bengt Pettersson, Mr. Jimmy Johansson at GKN Aerospace Sweden AB, and Mr. Fredrik Olofsson at Brogren Industries AB. We also appreciate the support from VDM Metals International in providing the material. Special acknowledgment to Mattias Igerstand from University West for performing the force TIG welding operations.

6. Contact Author Email Address

Mail to: achmad.ariaseta@hv.se or joel.andersson@hv.se

7. Copyright Statement

References

[1] Donachie M. J . and Donachie S. J. , Superalloys: a technical guide. ASM international, 2002.
[2] Sims C. T., Stoloff N. S., and Hagel W. C., superalloys II. Wiley New York, 1987.
[3] Reed R. C., The Superalloys: Fundamentals and Applications. Cambridge: Cambridge University Press, 2006.
[4] Fedorova T., J. Rösler, Gehrmann B., and Klöwer J., "Invention of a New 718-Type Ni-Co Superalloy Family for High Temperature Applications at 750° C," in 8th International Symposium on Superalloy 718 and Derivatives, 2014: Wiley Online Library, pp. 587-599.
[5] Fedorova T., Rösler J., Klöwer J., and Gehrmann B., "Development of a new 718-type Ni-Co superalloy family for high temperature applications at 750◦ C," in MATEC web of conferences, 2014, vol. 14: EDP Sciences, p. 01003.
[6] Rösler J., Hentrich T., and Gehrmann B., "On the Development Concept for a New 718-Type Superalloy with Improved Temperature Capability," Metals, vol. 9, no. 10, p. 1130, 2019.
[7] Solís C., Munke J., Bergner M., Kriele A., Mühlbauer M., Cheptiakov D., Gehrmann B., Rösler J., and Gilles R., "In Situ Characterization at Elevated Temperatures of a New Ni-Based Superalloy VDM-Alloy 780 Premium," Metallurgical and Materials Transactions A, vol. 49, no. 9, pp. 4373-4381, 2018.
[8] Andersson J., Weldability of precipitation hardening superalloys–influence of microstructure. Chalmers University of Technology, 2011.
[9] Andersson J., "Review of Weldability of Precipitation Hardening Ni-and Fe-Ni-Based Superalloys," in Proceedings of the 9th International Symposium on Superalloy 718 & Derivatives: Energy, Aerospace, and Industrial Applications, 2018: Springer, pp. 899-916.
[10] Khan A., Hilton P., Blackburn J., and Allen C., "Meeting weld quality criteria when laser welding Ni-based alloy 718," in International Congress on Applications of Lasers & Electro-Optics, 2012, vol. 2012, no. 1: Laser Institute of America, pp. 549-557.
[11] Eriksson L., Johansson E., Kettaneh-Wold N., Wikström C., and Wold S., "Design of experiments," Principles and Applications, Learn ways AB, Stockholm, 2000.